

Body-Area Powering With Human Body-Coupled Power Transmission and Energy Harvesting ICs

Jiamin Li, *Student Member, IEEE*, Yilong Dong, *Student Member, IEEE*, Jeong Hoan Park, *Member, IEEE*, Longyang Lin ^{id}, *Member, IEEE*, Tao Tang ^{id}, *Member, IEEE*, and Jerald Yoo ^{id}, *Senior Member, IEEE*

Abstract—This paper presents the body-coupled power transmission and ambient energy harvesting ICs. The ICs utilize human body-coupling to deliver power to the entire body, and at the same time, harvest energy from ambient EM waves coupled through the body. The ICs improve the recovered power level by adapting to the varying skin-electrode interface parasitic impedance at both the TX and RX. To maximize the power output from the TX, the dynamic impedance matching is performed amidst environment-induced variations. At the RX, the Detuned Impedance Booster (DIB) and the Bulk Adaptation Rectifier (BAR) are proposed to improve the power recovery and extend the power coverage further. In order to ensure the maximum power extraction despite the loading variations, the Dual-Mode Buck-Boost Converter (DM-BBC) is proposed. The ICs fabricated in 40 nm 1P8M CMOS recover up to 100 μ W from the body-coupled power transmission and 2.5 μ W from the ambient body-coupled energy harvesting. The ICs achieve the full-body area power delivery, with the power harvested from the ambience via the body-coupling mechanism independent of placements on the body. Both approaches show power sustainability for wearable electronics all around the human body.

Index Terms—Body area network, body-coupled power transmission, body-coupled energy harvesting, energy harvesting, power transfer, impedance matching, rectifier, maximum power point tracking.

I. INTRODUCTION

POWERING wearable electronics such as earbuds, smart band-aids, and electrocardiography (ECG) sensors are challenging [1]–[3]. The limited battery lifetime incurs charging overhead, causes service disruptions, and inconveniences the

Manuscript received July 20, 2020; revised September 4, 2020; accepted September 28, 2020. Date of publication November 20, 2020; date of current version December 30, 2020. This work was supported in part by A*STAR AME Nanosystems at the Edge Program under Grant A18A4b0055 and in part by National University of Singapore (NUS) under Grant R-263-000-C62-133/731. (Jiamin Li and Yilong Dong contributed equally to this work.) (Corresponding author: Jerald Yoo.)

Jiamin Li, Yilong Dong, Longyang Lin, and Tao Tang are with the Department of Electrical and Computer Engineering, National University of Singapore, Singapore 117583, Singapore (e-mail: jiamin.li@u.nus.edu; ydong@u.nus.edu; elelilo@nus.edu.sg; elett@nus.edu.sg).

Jeong Hoan Park was with the Department of Electrical and Computer Engineering, National University of Singapore, Singapore 117583, Singapore. He is now with Samsung Electronics, Hwaseong, Korea (e-mail: jh920.park@samsung.com).

Jerald Yoo is with the Department of Electrical and Computer Engineering, National University of Singapore, Singapore 117583, Singapore, and also with the N.I Institute for Health, Singapore 117456, Singapore (e-mail: jyoo@nus.edu.sg).

Color versions of one or more of the figures in this article are available at <https://doi.org/10.1109/TBCAS.2020.3039191>.

Digital Object Identifier 10.1109/TBCAS.2020.3039191

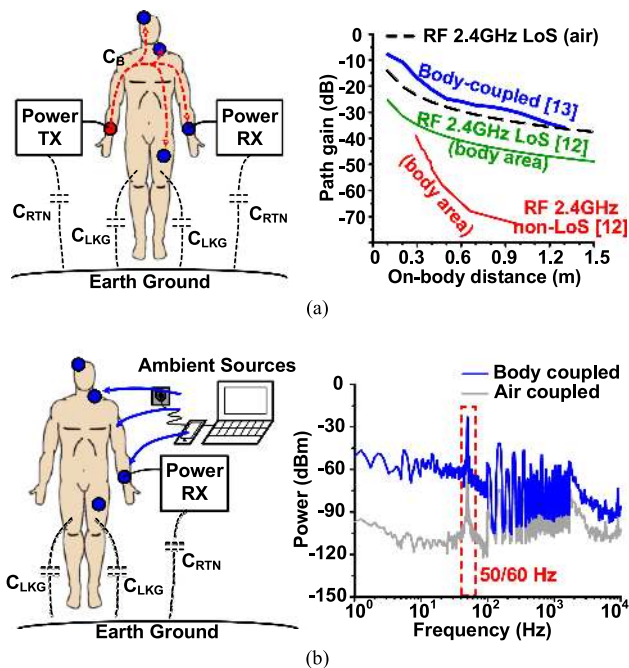


Fig. 1. Human body-coupled: (a) power transmission (where the body-coupled path gain is reported at 33 MHz [13]); (b) energy harvesting.

users [4], [5], which is aggravated further as the number of wearables increases. To address the issue and allow for sustainable operations, power transmission and energy harvesting approaches have been proposed.

Near-field power transmission approaches using the inductive link impose stringent requirements on the alignment and are typically designed for short distances. A self-localization and configuration scheme was adopted to alleviate the misalignment [6]–[8], but the approach applicability is still confined to the receiving nodes underneath the eTextiles shirt. RF-based power transmission covers a longer distance. However, when used in the body area, it experiences ~ 20 dB path loss degradation with the antenna pattern distorted, and a further 20–40 dB reduction in the path gain under non-line-of-sight (non-LoS) transmission, where the human body blocks the propagation path (Fig. 1(a)) [9]–[13]. This path loss alone hinders multiple nodes (e.g., placed >60 cm away) from receiving efficient power coverage. On the other hand, conventional energy harvesting approaches are effective only for particular locations on the body. While photovoltaics harvesting is used for sensors with

direct exposure to daylight [14], electrostatics-based harvesters (e.g., piezoelectric and triboelectric generators) operate at joints or underfoot [15], [16]. Harvesting from EM waves in the air is subject to the body positioning against the source, again due to the degradation caused by the body shadowing/blockage [17].

In this work, we use the body-coupling mechanism for power transmission and ambient energy harvesting to cover the entire body area. The return path is completed by the parasitic capacitance formed via the ground plane-to-Earth ground coupling (hence, there is no explicit closed loop formed to ensure safety). For the body-coupled power transmission, the path gain [13] (measured at 33 MHz) is up to 60 dB better than the 2.4 GHz RF non-LoS transmission in the body area and is insusceptible to body blockage (Fig. 1(a)). Meanwhile, the low-frequency EM wave existed in the ambiance is observed to couple onto the human body (Fig. 1(b)). Up to 30 dB higher EM strength is achieved with the body-coupling, as compared to that measured in the air. While the spectrum of low-frequency EM waves exhibits potentials for harvesting, the 50/60 Hz wave dominates and becomes the main source of energy harvesting.

Current attempts of the body-coupled power transmission are confined to the on-body distance of 30 cm or below [19]. To extend the coverage to the entire human body, key design challenges induced by the system characteristics need to be addressed. First, unlike conventional impedance matching with well-defined electrical nodes, both TX and RX interface with the indeterminate parasitic capacitance which varies with the environment, individual, skin-electrode interface and the transmission path. Second, due to the small return path parasitic capacitance (<1 pF) [10], [20] and thus the high impedance to be matched with, the trade-off between higher rectifier impedance and lower IR drop for better rectification efficiency needs to be dealt with. Third, the maximum load impedance needs to be dynamically tracked and maintained amidst impedance variations at the RX (harvester) front-end, to ensure optimal power extraction. This paper presents the TX and RX [21] ICs for the powering/harvesting via the body-coupling. In this paper, the dynamic impedance matching scheme is introduced at TX, while the detuned impedance booster (DIB), along with the bulk adaptation rectifier (BAR), is proposed at the RX, achieving the full-body area power coverage for the first time. The dual-mode buck-boost converter (DM-BBC) is introduced to ensure maximum power extraction despite impedance variations, for both the body-coupled power transmission and energy harvesting.

The paper is organized as follows. Section II characterizes the environmental impedance essential in the body-coupled power transmission and energy harvesting scheme, which guides the circuit design that follows. Section III presents the system architecture and overview. Section IV elaborates on the power transmitter (TX) circuit, and Section V describes the power receiver (RX) circuit. Section VI presents the on-body measurement results, and lastly, Section VII concludes the paper.

II. DESIGN CONSIDERATIONS

This section presents the characterization of the TX interface impedance and the RX optimum loading range. This information

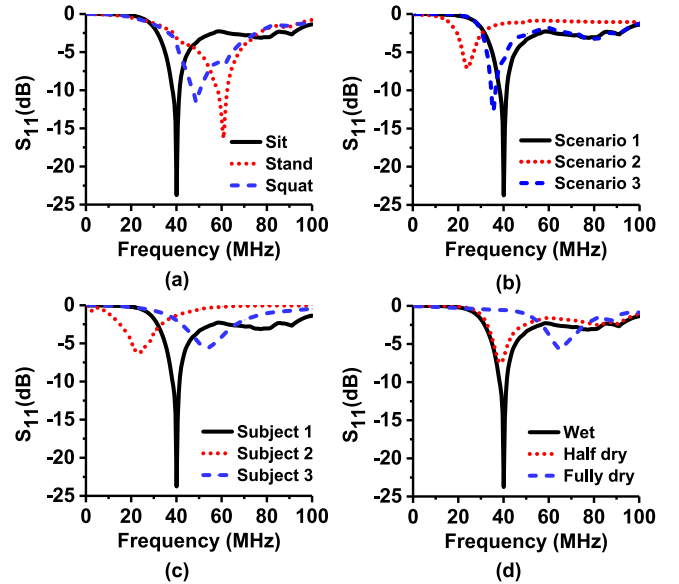


Fig. 2. Measured TX S_{11} variations due to: (a) human postures; (b) environmental conditions; (c) individual specificity; (d) skin-electrode contact conditions.

is essential for design choices, including TX matching strategy and scope, as well as the RX maximum power extraction scheme and parameter choice. The characterization is performed using the TX and RX rectifier design in this work. The body channel characteristics exploited in this work are similar to capacitive body coupled communication [18]. With the path loss characteristics discussed extensively in prior arts [10], [13], [20], [22]–[25], the transmission frequency is chosen to be 40 MHz.

A. TX Output Interface Impedance

The TX output interface is unconventional, with the load impedance contributed by the skin-electrode contact and the human body path impedance in its forward transmission direction, as well as the ground plane–Earth ground parasitic capacitance in its return path. When treated as a two-port network collectively, LC impedance matching could be performed to improve power transmission. Shown by the black curve in Fig. 2, the S_{11} parameter of -23 dB is achieved by the LC impedance matching (the structure and value selection of which will be elaborated in Section IV) at the transmission frequency of 40 MHz, on subject 3 in a sitting position wearing a wet electrode. However, due to the impedance variations induced by posture, environment, individual and electrode contact changes (the range of which will be elaborated in Section IV, Fig. 6), the S_{11} behavior is changed and is observed to degrade by up to 20 dB at 40 MHz from Fig. 2, when the fixed LC values are used. Therefore, to enhance the matching robustness and to ensure sufficient TX output power in practical scenarios of varying parasitic elements, the dynamic impedance matching and tracking become essential.

B. RX Optimal Loading

Fig. 3 illustrates the optimal RX loading variations under different power transmission conditions (e.g., different on-body

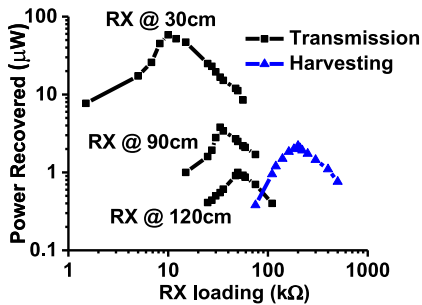


Fig. 3. Measured power recovery with respect to RX loading.

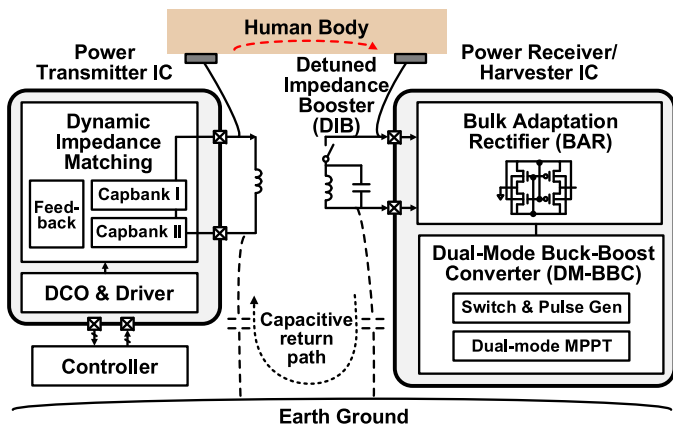


Fig. 4. System architecture.

transmission distances) or environmental variations, measured with the rectification front-end in this design. For the body-coupled power transmission, the optimal load resistance is measured to range from 10 k Ω to 50 k Ω . For the body-coupled ambient energy harvesting, the optimal resistance is observed to fall in a distinct range of around 150 k Ω to 300 k Ω . Both measurements are performed under different environments, postures, transmission distance and electrode placements in order to find a range to guide the RX loading design (i.e., converter equivalent input impedance). To ensure the power extraction with the optimal efficiency for nodes all around the body, maximum power point tracking (MPPT) is performed dynamically in the aforementioned range.

III. SYSTEM ARCHITECTURE

The system architecture is illustrated in Fig. 4. To improve the power recovery of the body-coupled power transmission, the dynamic impedance matching at the environment interface is performed at the TX. At the RX front-end, the detuned impedance booster (DIB) and the bulk adaptation rectifier (BAR) are proposed, further enhancing the power recovered and extending the power coverage to the full-body area. For the body-coupled energy harvesting, the DIB is disconnected, with the BAR still in operation for the power recovery. To ensure the optimal power extraction for both the transmission and harvesting with distinct MPP ranges, the dual-mode buck-boost converter (DM-BBC) is proposed to perform maximum power point tracking and load regulation at 1.1 V.

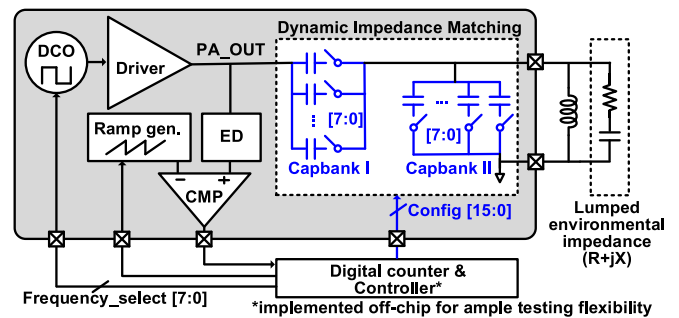


Fig. 5. TX block diagram with the lumped environmental impedance.

IV. POWER TRANSMITTER (TX) WITH DYNAMIC IMPEDANCE MATCHING

Fig. 5 illustrates the TX block diagram. The digitally controlled oscillator (DCO) generates the 40 MHz square wave, which then goes through a driver with the output impedance of 50 Ω . To enhance power transmission efficiency, the impedance matching network is introduced in between the driver output and the electrode interface. While the capbank I offers the adjustable capacitive element, the capbank II and the off-chip inductor are used jointly as the equivalent inductive element needed for impedance matching. This avoids the usage of an inductor bank [26], which is not only impractical for on-chip integration, but also bulky for wearable applications when implemented off-chip, considering the LSB to be in the hundred nH range at the transmission frequency of 40 MHz.

To maintain optimal power transmission amidst environmental impedance variations at the TX output interface, the dynamic matching is performed, which automatically configures the capbank I and II. Upon the matched impedance where the driver output impedance equals the equivalent load impedance, half of the driver's open-circuit voltage falls across the load. Therefore, the envelop detector (ED) [27] is used to track the driver output amplitude (which will be affected by the capbank configurations), which is then compared with a ramp waveform for the voltage-time conversion using a digital counter. Such time information represented by the number of counting cycles provides feedback to the digital controller and guides the capbank reconfiguration direction, until the driver output amplitude eventually approaches half the open circuit amplitude.

The TX-body/environment is considered as a two-port network, with the output interface (incorporating both the forward transmission path and the return path impedance) measured as a whole. Different environmental settings, subjects, postures, skin-electrode interface conditions, and electrode placements are applied to find the range. As shown in red in Fig. 6, the resistive component is expected to range from 2 k Ω to 30 k Ω , and the capacitive component from 0.1 pF to 7 pF. To ensure that these potential impedances are covered by the matching network designed, the two capacitor banks have an 8-bit configurability with the LSB controlling 50 fF. The off-chip inductor is 2.2 μ H. Fig. 6 (blue) illustrates the coverage designed by the matching network.

With 65,536 ($2^8 \times 2^8$) possible capacitor configurations, the 2-dimensional dichotomy-based searching method is

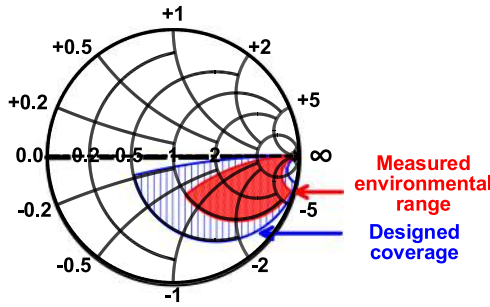


Fig. 6. Measured environmental impedance range and the coverage by the matching network designed.

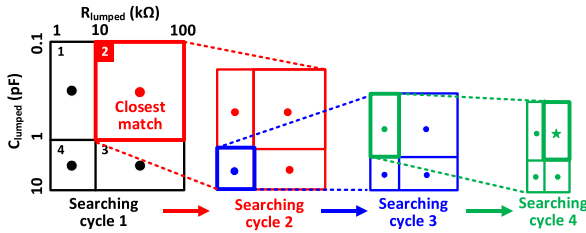


Fig. 7. Operation of the dichotomy searching method.

proposed, to expedite the final convergence (Fig. 7). The potential environment-equivalent resistance and capacitance ranges are represented by a 2-dimensional searching plane, with the vertical axis being the capacitive element and the horizontal axis being resistive. Each point on the plane thus represents one possible environmental impedance. During the first searching cycle, the plane is divided into 4 quadrants, with the capbank configured to match each center point sequentially. Upon deciding the closest match (by comparing the driver output amplitude against half the open circuit amplitude), its corresponding quadrant is selected for further sub-divisions. This process is repeated until the driver output amplitude reaches half the open circuit amplitude with ± 0.15 V tolerance. The maximum searching cycle (i.e., plane/quadrant sub-division) is limited to 4, corresponding to 16 times output amplitude evaluation and thus the worst settling time of 16 ms (where the interval in between two evaluations is 1 ms). Assuming slower environmental impedance change (> 100 ms, as the human body movement is generally below 10 Hz), there will not be instability concerning the algorithm. Fig. 8 shows the measured transient behavior of the TX output power and the driver output amplitude during the searching procedure. In this figure, a capbank configuration initially matched under one environmental setting is subject to interface impedance changes. As a result, the TX driver output amplitude drifts away from half its open circuit amplitude (1.25 V), and thus triggering the searching for a new matched capbank configuration and resulting in a 7.5X output power improvement.

V. POWER RECOVERY RECEIVER (RX) DESIGN

A. Detuned Impedance Boosting (DIB)

Illustrated in Fig. 9(a), the parasitic capacitance C_{RTN} formed by the ground plane to the Earth ground coupling completes the circuit loop and contributes positively to the power recovery. Generally, below 1 pF, the C_{RTN} is the largest environmental

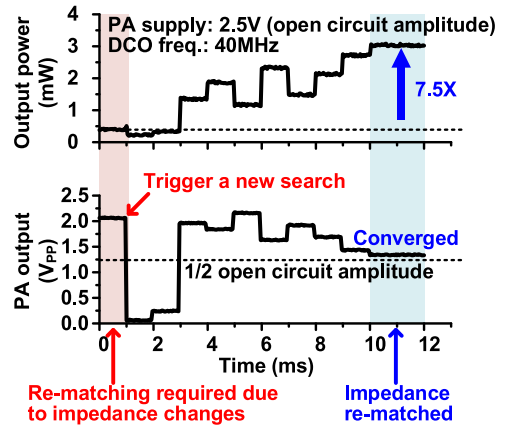


Fig. 8. Measured transient waveforms of the dynamic impedance matching.

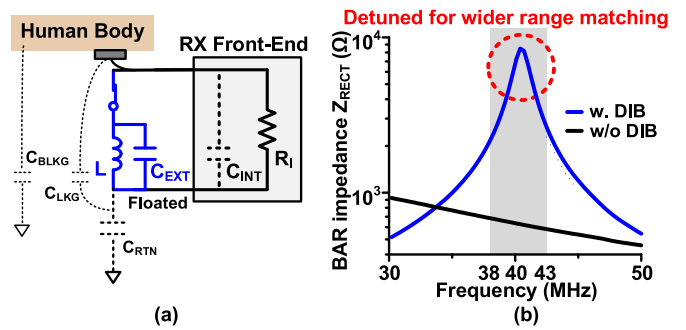


Fig. 9. Illustration and measurements of the RX input impedance with and without the detuned impedance booster (DIB).

impedance drawing away the voltage and power from the RX input, whereas others such as skin-electrode interface exhibits ~ 100 nF parallel capacitance (using the wet electrode 3M 2237) and an overall impedance of $\sim 130 \Omega$ at 40 MHz. Shown in Fig. 9(b), the RX input impedance is measured to be $\sim 600 \Omega$ at 40 MHz (~ 10 times lower than the fF-level C_{RTN}), resulting in the low input voltage and power observed at the RX front-end. On top of the degraded power transmission efficiency, the low input voltage also leads to low rectification efficiency due to the threshold drop.

With the C_{RTN} being the dominant factor, the parallel LC impedance boosting circuit is introduced at the RX front-end. The inductor resonates with the overall capacitance of both the external capacitor C_{EXT} and the equivalent rectifier input capacitor C_{INT} , to boost the RX input impedance at 40 MHz. The inductor is $1.2 \mu\text{H}$ and the capacitor is 6.8 pF, so that the boosted RX input impedance is measured around 8 k Ω (Fig. 9), which is around the same level as the impedance of C_{RTN} at the resonance/transmission frequency of 40 MHz. This not only increases the voltage received at the RX, but also enhances the impedance matching for more efficient power transmission. In addition, to cope with environmental variation widely observed in the body area, we intentionally detune the LC tank for impedance matching across a wider range. Around 6-10X impedance boosting could be observed across a 2.8 MHz bandwidth, in order to improve its robustness against capacitance variations due to environmental, individual, or setup changes.

B. Bulk Adaptation Rectifier (BAR)

As the on-body transmission distance increases to 120 cm, the amplitude received after the TRX impedance matching and boosting will drop below 0.3 V, which is in the subthreshold region of a MOSFET. To improve the drain current (i.e., conduction current) for higher power efficiency, techniques to compensate V_{TH} have been proposed [28]. “Static” V_{TH} compensation uses a small DC voltage to facilitate gate biasing, which could be generated by an external supply (e.g., a small battery or harvesters) on a switched capacitor [29], or internally from the rectifier output (e.g., bootstrapping [30]). However, while the static biasing increases the forward conduction current, its indiscriminate V_{TH} compensation also leads to higher reverse leakage current, which limits the improvement in the power conversion efficiency (PCE). On the other hand, the cross-coupled differential-drive rectifier uses the input AC voltage to “dynamically” bias the gate voltage [28]. It raises the $|V_{GS}|$ for MOSFETs in the forward conduction path while suppressing it for those in the reverse leakage path. With I_D positively correlated with $(V_{GS}-V_{TH})$, the conduction current is improved with the leakage current reduced.

However, when the input amplitude is smaller than 0.3 V, the largest “dynamically” biased V_{GS} using the differential-drive rectifier is smaller than 0.6 V, which is around the MOSFET threshold. To further improve the power recovery at such low input amplitudes, more aggressive V_{TH} cancellation is needed. While most works have mainly focused on compensating V_{GS} , we propose the Bulk Adaptation Rectifier (BAR) which adaptively introduces the bulk biasing for dynamic V_{TH} alteration at low input amplitude on top of the dynamic V_{GS} .

Fig. 10 shows the operation of the proposed BAR. When the input amplitude drops below 0.6 V, M5-M8 are turned on, which connects the bulk of M1-M4 towards V_{IP} and V_{IM} , allowing their bulk voltages to alter dynamically based on the AC input. Note that M3 and M4 are deep n-well transistors. During the half-sine cycle where V_{IP} is higher than V_{IM} , M1 and M3 are in the forward conduction path and are forward bulk biased. Their threshold voltage is thus reduced, allowing more forward conduction current to V_{RECT} . On the other hand, M2 and M4 are in the leakage path and are reverse bulk biased, with an increased threshold to suppress the leakage current flow out of V_{RECT} . The same applies to the other sine cycle where $V_{IM} > V_{IP}$. In this mode, the source/drain-bulk DC leakage current due to the bulk potential adjustment is increased, but still 4-6 orders of magnitude lower than the conduction current. The more prominent AC leakage due to bulk capacitance (not caused by the bulk adaption proposed) will be directed towards V_{RECT} (elaborated later in the normal mode) before it degrades the power recovery.

At higher input amplitude (>0.6 V), the dynamic V_{GS} is much greater than V_{TH} . Meanwhile, the body diodes start to approach their turn-on voltage and cause increased leakage, making the bulk biasing no longer necessary nor efficient. Therefore, M5-M8 reconfigure the bulk of M1-M4 towards V_{RECT} and ground, similar to the conventional differential-drive structure. This aligns the body diode towards the V_{RECT} , which effectively avoids leakage via the body diode. The “MODE” is

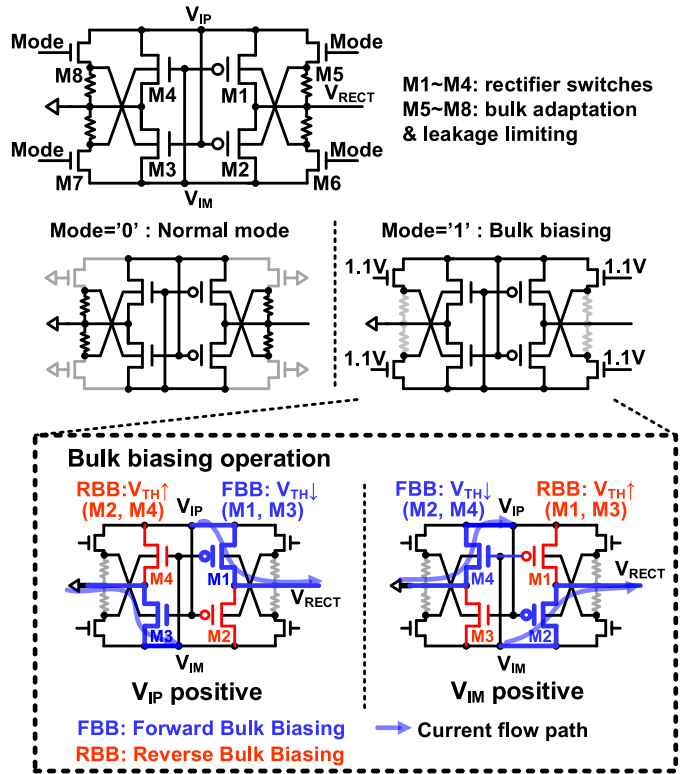


Fig. 10. Bulk Adaptation Rectifier (BAR) operating principle.

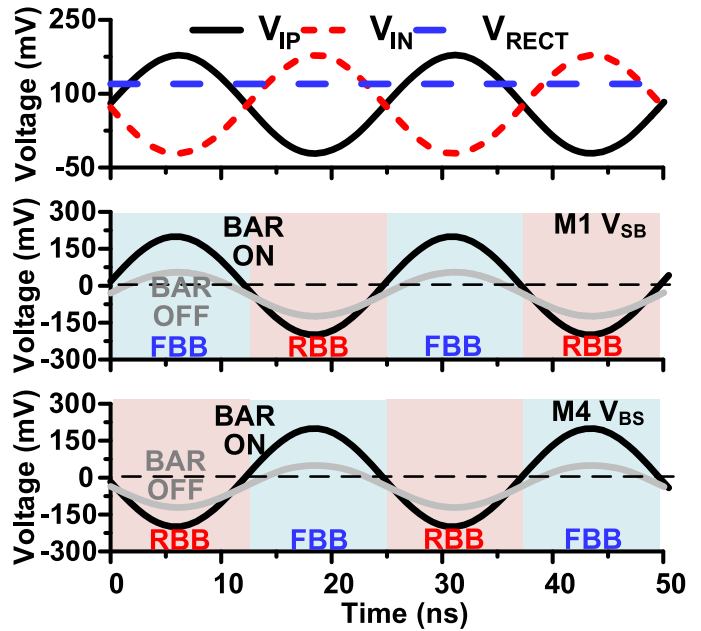


Fig. 11. Simulated source-bulk potentials during the BAR operation.

determined by the comparison between V_{RECT} and the reference voltage 0.4 V (assuming the optimal load is achieved by the next-stage converter), using a duty-cycled dynamic comparator. The average power is 8.5 nW.

Fig. 11 shows the V_{SB}/V_{BS} (for PMOS and NMOS, respectively) behavior using the BAR. With an input amplitude of 200 mV, the circuit operates in the bulk biasing mode. As compared to the conventional differential-drive rectifier, the V_{SB}/V_{BS} is

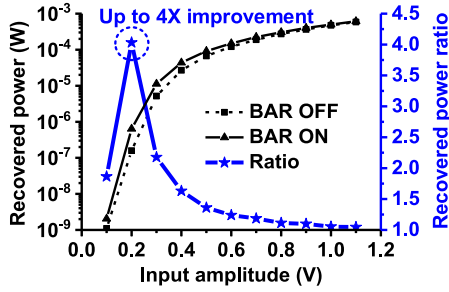


Fig. 12. Measured power recovery enhancement by BAR compared to conventional rectifiers.

improved for transistors along the forward conduction path, and decreased for those along the reverse leakage path.

As the RX interfaces with the skin and the parasitic capacitance with the Earth ground, the exact input power is unknown due to the undetermined source impedance, making PCE calculation and comparison impractical. Rather, we show directly the power recovery on human body with and without the rectifier improvements in Section VI. Fig. 12 here illustrates the ratio of measured power recovery by the BAR to that when the bulk biasing is turned off.

C. Dual-Mode Buck-Boost Converter (DM-BBC)

As discussed in Section II, the optimal impedance range for the maximum power extraction at the RX is 10 k Ω –50 k Ω for the body-coupled power transmission, and 150 k Ω –300 k Ω for the body-coupled ambient energy harvesting. Despite its range being measured and estimated, the exact impedance varies with the environment, individual and path characteristics. With the recovered voltage ranging from 0.2 V to 1.5 V, a buck-boost converter is required 1) to have an equivalent input impedance which dynamically adapts to the harvester impedance in real time; 2) to regulate the RX load to a constant 1.1 V – the nominal supply voltage for standard MOSFETs in 40 nm.

Several MPPT techniques have been proposed in the literature [31]–[34]. For a majority of energy harvesting applications (e.g., photovoltaics, triboelectric and biofuel harvesting), the MPP occurs (i.e., the converter equivalent input impedance matches with the source impedance) when the converter input voltage is kept at a fixed and pre-determined fraction of its open circuit voltage (OCV). The OCV could be measured in real time, either by a replica harvesting circuitry [31] or by periodic sample and hold on a capacitor [32]. While a replica could reflect the OCV of the actual harvester for applications like photovoltaics as long as the identical lighting conditions are ensured, it would reduce the RX input impedance and contribute to leakage if introduced in parallel at the RX front-end. The periodic sample and hold of the OCV is also not ideal, as it disrupts the harvester operation. On the other hand, the power monitor loop proposed in [33] uses T2 (the inductor discharging time) as the feedback to guide the MPPT direction, based on the positive correlation between P_{IN} and T2 at a fixed frequency. This technique utilizes only existing parameters and thus does not affect the normal operation. However, for our application where the harvester impedance spans from 10 k Ω to 300 k Ω , using the power monitor

loop solely for MPPT would result in an increased T1 (the inductor charging time) range, degrading the resolution and the settling time during the mode switching.

To address the aforementioned issues, the Dual-Mode Buck-Boost Converter (DM-BBC) operating in the discontinuous conduction mode (DCM) is introduced, as illustrated in Fig. 13. The DCM time T0 is adaptable to the converter input power P_{IN} (in 4 configurations), and is designed to increase at lower P_{IN} (elaborated later). Meanwhile, this T0 is utilized for the converter impedance to settle down fast to the mean MPP, after which the impedance monitor loop (using T2 as the feedback) [33] adjusts T1 dynamically to fine-tune the MPP, with the step size of 12 ns and 32 steps in total. The effect of T0 and T1 on the converter impedance is expressed by

$$Z_{DM_BBC} = 2L \cdot T_{SW}/T1 \approx 2L \cdot T0/T1 \quad (1)$$

where L is the inductance and T_{SW} is the switching period. T0 dominates the T_{SW} by being larger than T1 and T2 by ~ 7 –4000X in this design, and thus the approximation above. The relationship between P_{IN} and T2 for the buck-boost converter is given by

$$P_{IN} = V_{IN} \cdot \overline{I_{IN}} = \left(\frac{V_{OUT} \cdot T2}{T1} \right) \cdot \left(\frac{V_{IN} \cdot T1}{2L \cdot T_{SW}} \right) \\ \approx \frac{T2 \cdot V_{IN} \cdot V_{OUT}}{2L \cdot T0}$$

Therefore, T2 is positively proportional to P_{IN}. Assuming that V_{IN} varies slower than 20 ms (10T_{SW,MAX}), with V_{OUT} and L fixed, and T0 maintained the same for each configuration, T2 then serves as the indicator of P_{IN} level to guide the T1 adjustment direction for MPP fine-tuning.

The converter operates asynchronously to suppress quiescent current. The pulse generation involving T0, T1, and T2 self oscillates [31], [35], as long as V_{OUT} drops below 1.1 V (with \overline{EN} held to 0, which is decided by a continuous-time comparator) which indicates the need of power delivery to the load. The maximum conversion frequency f_{SW} is 1/(T0 + T1 + T2), where T0 dominates. The conversion frequency is adaptively reduced under lighter loading conditions, with the pulse generation halted upon V_{OUT} charged over 1.1 V. T1 and T2 are generated by tunable RC delay lines [31], [35], [36]. While the duration of T1 is determined by the MPPT, the T2 duration is decided by zero current switching (ZCS) [31], [35]. T0 is generated by the tunable capacitor charging by a leakage-based current reference [37]. The Adaptive Level Shifter (ALS) is introduced so that PM1 can be fully turned off when V_{IN} > 1.1 V. The schematic is shown in Fig. 13(d), where the dynamic comparator triggered by the PHI1 falling edge compares half V_{IN} against the reference voltage 0.55 V. V_{VIRT} takes on the higher potential between V_{IN} and V_{DD}, and is used as the supply for PHI1 generation. A level-shifter is required here to turn off the header PM1 when V_{VIRT} is higher than 1.1 V. With several start-up techniques in the literature applicable [38]–[40], the start-up circuit is not included in this system.

To improve both the conversion and MPPT efficiency, T0 is first optimized with respect to the input voltage and power, illustrated in Fig. 14. It is observed that the optimal f_{SW} increases

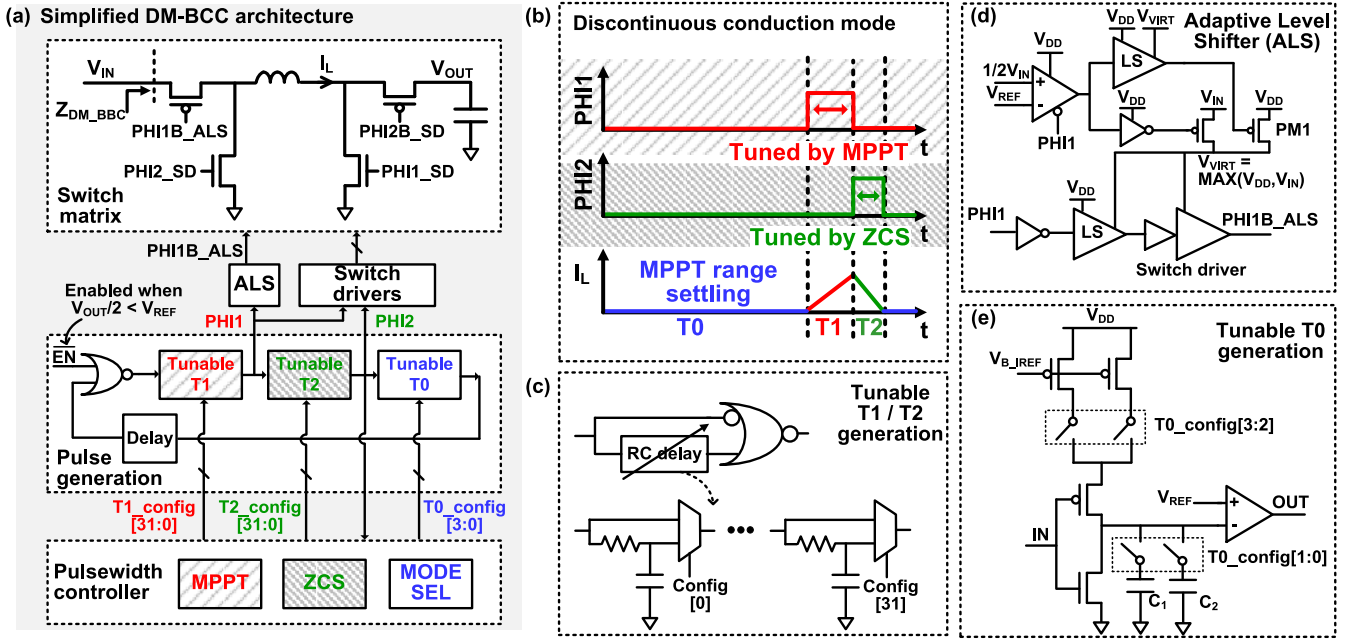
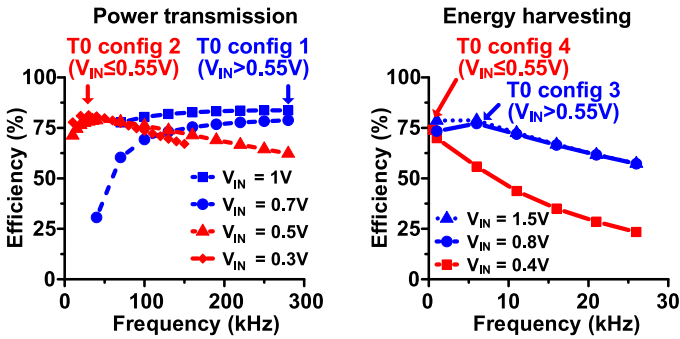


Fig. 13. Dual-Mode Buck-Boost Converter (DM-BBC) structure.


 Fig. 14. T_0 optimization with respect to input voltage.

under higher input voltage, and vice versa. This is because that at the rectifier load (converter input impedance Z_{DM_BBC}), the optimal impedance decreases at higher input voltage as observed in this application (due to higher I_{ON} and lower rectifier impedance). This then leads to higher current into the converter and thus higher conduction loss. To balance it with the switching loss for the maximum conversion efficiency [36], f_{SW} needs to be increased. Therefore, f_{SW} adapts to 15 kHz and 280 kHz in the power transmission mode, and 500 Hz and 6 kHz in the energy harvesting mode by changing the T_0 for better conversion efficiency. T_1 is then determined by (1) to range from 100–480 ns, so that the target Z_{DM_BBC} span could be covered. The switch sizing is also optimized by balancing the switching and conduction loss, with larger switches leading to higher switching loss but lower conduction loss, and vice versa [36].

Fig. 15 illustrates the asynchronous MPPT operation (which could be implemented and synthesized with standard cells). Upon T_2 being updated by ZCS, the completion status of T_2 adjustment under a given T_1 is determined. T_1 is then updated only if the T_2 is settled and the converter operates at the maximum frequency f_{SW} . Comparing the currently settled T_2 with

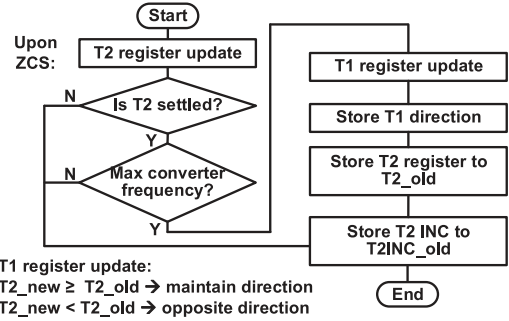


Fig. 15. MPPT operation flow chart.

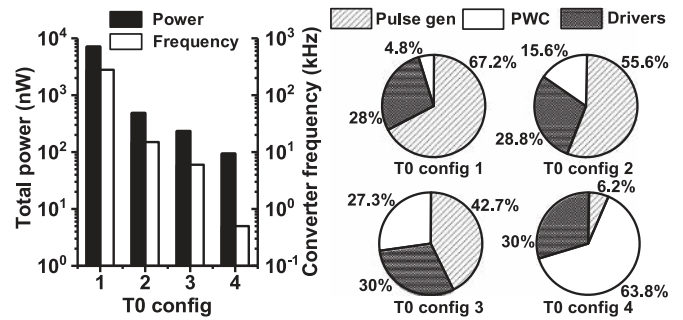


Fig. 16. Measured DM-BBC total power consumption, switching frequency and power breakdown at different configurations.

the stored value, T_1 increment/decrement direction is stored, along with the current T_2 value and the ZCS decision. Cycle check is performed at last and ‘ T_2 unsettled’ is assumed at the following cycle, should this be the first T_2 value under the newly changed T_1 .

The power consumption and breakdown of the converter are illustrated in Fig. 16. As T_0 increases at lower input power, the total power consumption is measured to be $7.14 \mu\text{W}$, 486 nW ,

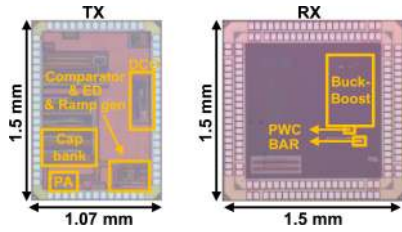


Fig. 17. Chip micrograph of the TX and RX.

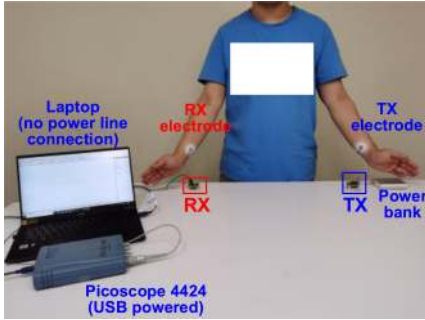


Fig. 18. Measurement setup.

234 nW, and 94 nW under the 4 configurations, respectively. The reduction is contributed by both decreased switching activities, and the lower bias current for continuous-time comparators due to higher delay tolerance at larger T₀. The percentage of pulse width controller (PWC) power takes the dominance as its active power gradually approaches its quiescent power of ~60 nW, whereas the driver and pulse generation power still see a decrease (with a quiescent power of 17 nW). As compared to the recovered power range of >30 μW and 800 nW-30 μW for power transmission, and >1 μW and 130 nW-1 μW for the harvesting, the converter power consumption is affordable.

VI. ON-BODY MEASUREMENT RESULTS

Fig. 17 shows the chip microphotograph of the TX IC and the RX IC, designed for the body-coupled power transmission and ambient energy harvesting. They are fabricated in the 40 nm CMOS technology, with the TX IC occupying 0.21 mm² and the RX IC 0.29 mm². Off-chip components required for the design include the inductor used for TX impedance matching, the LC tank (1.2 μH, 6.8 pF) for DIB at the RX front-end, and the converter inductor (47 μH).

Measurements of the power recovery have been performed on the human body, with the wet electrodes (Red dot, 3M Ag/AgCl, 2237) used as the interface to couple the electric field onto and from the skin surface. The measurement setup is shown in Fig. 18, where the TX is battery powered, and the USB-powered picoscope is used to avoid additional return path coupling induced by equipment. The laptop is not connected with the power line, which is also to avoid the additional return path parasitic. Both TX and RX PCB are 4 x 4 x 1 cm³.

With the TX impedance matching, the power recovery could be improved by >3X while the coverage be extended by 4X (Fig. 19). Shown in Fig. 20, with the TX placed on the subject's wrist outputting ~3 mW, the RX power recovery at 15 cm

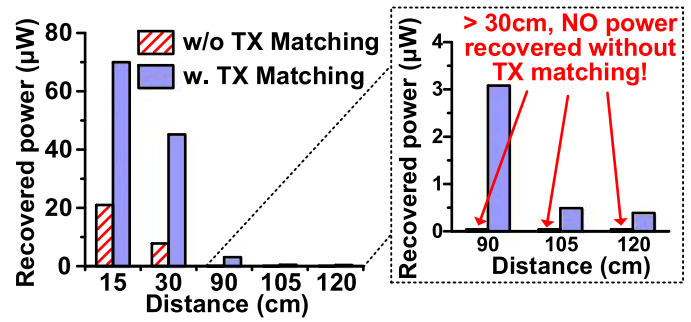


Fig. 19. Measured recovered power with and without TX matching.

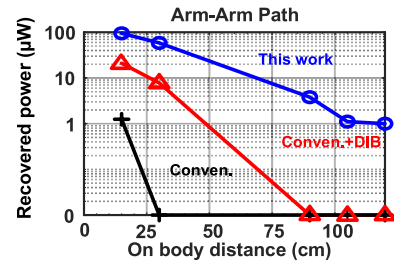


Fig. 20. Measured recovered power along the arm-arm path.

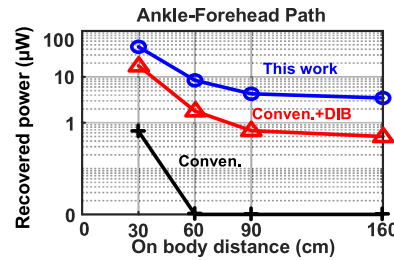


Fig. 21. Measured recovered power along the ankle-forehead path.

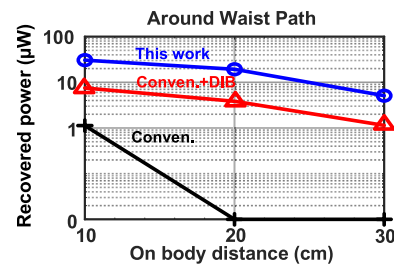


Fig. 22. Measured recovered power around the waist.

apart along the arm is improved from 1.3 μW to 100 μW in this work, as compared to the power transmission using the TX and a conventional differential drive rectifier of the same size. Meanwhile, at ~120 cm apart where the RX node is placed on the other wrist, 1 μW could still be recovered, extending the coverage by 8 times. Fig. 21 shows the power recovery at RX nodes along the ankle-to-forehead path, with the TX placed on the subject's forehead. With the RX placed at 160 cm apart on the subject's ankle, slightly higher power (than expected) is recovered. This could be due to the increased return path

TABLE I
 PERFORMANCE COMPARISON WITH PREVIOUS BODY-AREA POWERING WORKS

	This Work	JSSC'20 [16]	JSSC'19 [41]	JSSC'18 [34]	JSSC'14 [8]	JSSC'14 [32]
Process	40nm	180nm BCD	180nm	28nm	180nm	65nm
Harvester	Body-coupled power transmission & harvesting	Tribo	Thermal	PV + TEG + BFC + battery	Wireless-wireline inductive transfer	Far-field RF harvesting
Operating Frequency	Transmission: 40 MHz Harvesting: e.g., 50/60 Hz	100 Hz	NA	NA	1 MHz	904.5 MHz
TX Power	Transmission: 3 mW Harvesting: N.A.	NA	NA	NA	2.9 mW	20 dBm
Recovered Power	Transmission: 100 μ W Harvesting: 2.5 μ W	2-10uW*	<90uW*	1uW-60mW	34uW	231.6uW (<3m)
Converting Method	Rectifier + buck-boost converter	Rectifier + buck	Boost	Buck-Boost	Rectifier	Rectifier + boost
MPPT	T0 adaptation + hill climbing	Fractional V_{OC} [Fixed ratio]	Fractional V_{OC} [Fixed impedance]	Adaptive T_{ON} & F_{SW} [Known V_{MPP}]	NA	S/H for efficiency tracking
End-end Efficiency	Transmission: 3.3% (15 cm); 0.03% (160 cm)	N.A.	N.A.	N.A.	1.2% (<20 cm)	0.11% (3m)
Quiescent I	70nA; 73nA; 92 nA; 810 nA	251.5nA	N.A.	262nA	NA	<1uA
Coverage	Transmission: full body Harvesting: placement independent	Joints; feet	Placements with heat flow	Except for human torso	<20 cm facing sensor node	0.9-9m off-body (antenna dependent)
Area (mm ²)	TX:0.21; RX: 0.29	2.482	1.6	0.5	TX: 2.95; RX: 1.46	2

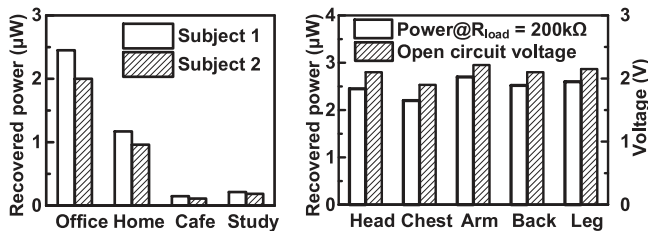


Fig. 23. Measured body-coupled harvested power in different environment and its placement independency.

coupling and was observed multiple times (in measurements and in a demonstration using a digital watch/calculator) when the RX was placed closer to the foot or the Earth ground. This work improves the power recovered at 30 cm from 650 nW to 45.2 μ W, and the coverage from 30 cm to 160 cm. The end-to-end efficiency from the TX output to the RX recovered power is calculated to be 3.3% at 15 cm apart and 0.03% at 160 cm apart. Along the non-LoS path of around the waist, the body-coupled approach delivers 5 μ W from the front to the back of the body.

Using the body-coupling mechanism to harvest the ambient EM waves in different daily environments, up to 2.5 μ W could be scavenged, illustrated in Fig. 23. While being environment-dependent (an intrinsic characteristic shared by all harvesters), the amount of power harvested is indifferent to where the RX node is placed on the human body despite slight fluctuations (Fig. 23). This placement independency is advantageous and unique, as it allows for the simultaneous energy scavenging by all wearable nodes, unlike conventional harvesters, which only operate for specific body area locations/postures.

In comparison with the state-of-the-art power transmission [8], [32] and harvesting [16], [34], [41] systems for wearable applications, this is the first work to utilize the body-coupling mechanism for full-range body area power transmission and harvesting (Table I). The harvesting scheme scavenges low-frequency EM waves, which could not be achieved by antenna-based RF harvesting due to the infeasible antenna sizing. The circuit techniques introduced allow for power extraction/recovery

by this mechanism in the similar ranges as the conventional ones, while being the only one which supports power delivery/energy harvesting to/across the entire body.

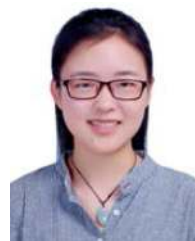
VII. CONCLUSION

We presented the TX and RX IC for power transmission and energy harvesting via the body-coupling mechanism. The characterization performed at the TX-environment interface and the RX loading motivates the circuit design. To mitigate the parasitic capacitance variation and to reduce the power reflection, the dynamic impedance matching with environmental parasitics is introduced at the TX output. At the RX, the detuned impedance matching and the bulk adaptation rectifier are proposed for improved power recovery and 8X enhancement in the on-body power transmission distance. The DM-BBC is designed to support dynamic MPPT and fast settling during mode transition. Overall, this work achieves full-body area power transmission and placement indifferent ambient energy harvesting, providing a sustainable powering solution for wearable nodes all around the human body.

REFERENCES

- [1] J. Yoo and H. J. Yoo, "Wearable healthcare system," in *Bio-Medical CMOS ICs*, Boston, MA, USA, Springer, 2011, pp. 339–370.
- [2] J. Wang *et al.*, "Sustainably powering wearable electronics solely by biomechanical energy," *Nat. Comm.*, 2016.
- [3] M. Schormans, V. Valente, and A. Demosthenous, "Practical inductive link design for biomedical wireless power transfer: A tutorial," *IEEE Trans. Biomed. Circuits Syst.*, vol. 12, no. 5, pp. 1112–1130, Oct. 2018.
- [4] M. Peng, K. Yan, H. Hu, D. Shen, W. Song, and D. Zou, "Efficient fiber shaped zinc bromide batteries and dye sensitized solar cells for flexible power sources," *J. Mater. Chem. C*, 2015.
- [5] K. Dong *et al.*, "A highly stretchable and washable all-yarn-based self-charging knitting power textile composed of fiber triboelectric nanogenerators and supercapacitors," *ACS Nano.*, 2017.
- [6] J. Yoo, S. Lee, and H. Yoo, "A 1.12 pJ/b inductive transceiver with a fault-tolerant network switch for multi-layer wearable body area network applications," *IEEE J. Solid-State Circuits*, vol. 44, no. 11, pp. 2999–3010, Nov. 2009.
- [7] J. Yoo, L. Yan, S. Lee, Y. Kim, and H. Yoo, "A 5.2 mW self-configured wearable body sensor network controller and a 12 μ W wirelessly powered sensor for a continuous health monitoring system," *IEEE J. Solid-State Circuits*, vol. 45, no. 1, pp. 178–188, Jan. 2010.

- [8] N. Desai, J. Yoo, and A. P. Chandrakasan, "A scalable, 2.9 mW, 1 Mb/s e-textiles body area network transceiver with remotely-powered nodes and Bi-directional data communication," *IEEE J. Solid-State Circuits*, vol. 49, no. 9, pp. 1995–2004, Sep. 2014.
- [9] S. L. Cotton, R. D'Errico, and C. Oestges, "A review of radio channel models for body centric communications," *Radio Sci.*, 2014.
- [10] Y. Kifle, H. Kim, and J. Yoo, "Human body and head characteristics as a communication medium for body area network," in *Proc. 37th Annu. Int. Conf. IEEE Eng. Med. Biol. Soc.*, 2015, pp. 1845–1848.
- [11] A. Fort, J. Ryckaert, C. Desset, P. De Doncker, P. Wambacq, and L. Van Biesen, "Ultra-wideband channel model for communication around the human body," *IEEE J. Sel. Areas Commun.*, vol. 24, no. 4, pp. 927–933, Apr. 2006.
- [12] P. S. Hall and Y. Hao, "Antennas and propagation for body centric communications," in *Proc. Eur. Conf. Antennas Propag.*, 2006, pp. 1–7.
- [13] J. Bae, H. Cho, K. Song, H. Lee, and H. Yoo, "The signal transmission mechanism on the surface of human body for body channel communication," *IEEE Trans. Microw. Theory Techn.*, vol. 60, no. 3, pp. 582–593, Mar. 2012.
- [14] P. Chen, C. Wu, and K. Lin, "A 50 nW-to-10 mW output power Tri-mode digital buck converter with self-tracking zero current detection for photovoltaic energy harvesting," *IEEE J. Solid-State Circuits*, vol. 51, no. 2, pp. 523–532, Feb. 2016.
- [15] D. Kwon and G. A. Rincón-Mora, "A single-inductor 0.35 μm CMOS energy-investing piezoelectric harvester," *IEEE J. Solid-State Circuits*, vol. 49, no. 10, pp. 2277–2291, Oct. 2014.
- [16] I. Park, J. Maeng, M. Shim, J. Jeong, and C. Kim, "A high-voltage dual-input buck converter achieving 52.9% maximum end-to-end efficiency for triboelectric energy-harvesting applications," *IEEE J. Solid-State Circuits*, vol. 55, no. 5, pp. 1324–1336, May 2020.
- [17] K. R. Sadagopan, J. Kang, Y. Ramadass, and A. Natarajan, "A 960pW co-integrated-antenna wireless energy harvester for wifi backchannel wireless powering," in *IEEE Int. Solid-State Circuits Conf. Dig. Tech. Papers*, vol. 61, pp. 136–138, Feb. 2018.
- [18] N. Cho, J. Yoo, S. Song, J. Lee, S. Jeon, and H. Yoo, "The human body characteristics as a signal transmission medium for intrabody communication," *IEEE Trans. Microw. Theory Techn.*, vol. 55, no. 5, pp. 1080–1086, May 2007.
- [19] H. Cho, J. Suh, H. Shin, Y. Jeon, C. Jung, and M. Je, "An area-efficient rectifier with threshold voltage cancellation for intra-body power transfer," in *Proc. IEEE Int. Symp. Circuits Syst.*, 2019, pp. 1–5.
- [20] T. G. Zimmerman, "Personal area networks: Near-field intrabody communication," *IBM Syst. J.*, vol. 35, no. 3–4, pp. 609–617, 1996.
- [21] J. Li *et al.*, "Human-body-coupled power-delivery and ambient-energy-harvesting ICs for a full-body-area power sustainability," in *IEEE Int. Solid-State Circuits Conf. Dig. Tech. Papers*, vol. 63, pp. 514–516, Feb. 2020.
- [22] W. Saadeh, M. A. B. Altaf, H. Alsuradi, and J. Yoo, "A 1.1-mW ground effect-resilient body-coupled communication transceiver with pseudo OFDM for head and body area network," *IEEE J. Solid-State Circuits*, vol. 52, no. 10, pp. 2690–2702, Oct. 2017.
- [23] J. Zhao *et al.*, "An auto loss compensation system for capacitive-coupled body channel communication," *IEEE Trans. Biomed. Circuits Syst.*, vol. 13, no. 4, pp. 756–765, Aug. 2019.
- [24] W. Sun, J. Zhao, Y. Huang, Y. Sun, H. Yang, and Y. Liu, "Dynamic channel modeling and OFDM system analysis for capacitive coupling body channel communication," *IEEE Trans. Biomed. Circuits Syst.*, vol. 13, no. 4, pp. 735–745, Aug. 2019.
- [25] W. Saadeh, M. A. B. Altaf, H. Alsuradi, and J. Yoo, "A pseudo OFDM with miniaturized FSK demodulation body-coupled communication transceiver for binaural hearing aids in 65 nm CMOS," *IEEE J. Solid-State Circuits*, vol. 52, no. 3, pp. 757–768, Mar. 2017.
- [26] B. Zhao, J. Mao, J. Zhao, H. Yang, and Y. Lian, "The role and challenges of body channel communication in wearable flexible electronics," *IEEE Trans. Biomed. Circuits Syst.*, vol. 14, no. 2, pp. 283–296, Apr. 2020.
- [27] N. M. Pletcher, S. Gambini, and J. M. Rabaey, "A 2 GHz 52 μW wake-up receiver with -72 dBm sensitivity using uncertain-IF architecture," *IEEE Int. Solid-State Circuits Conf. Dig. Tech. Papers*, vol. 51, pp. 524–633, Feb. 2008.
- [28] K. Kotani, A. Sasaki, and T. Ito, "High-efficiency differential-drive CMOS rectifier for UHF RFID," *IEEE J. Solid-State Circuits*, vol. 44, no. 11, pp. 3011–3018, Nov. 2009.
- [29] H. Nakamoto *et al.*, "A passive UHF RF identification CMOS tag IC using ferroelectric RAM in 0.35 μm technology," *IEEE J. Solid-State Circuits*, vol. 42, no. 1, pp. 101–110, Jan. 2007.
- [30] S. S. Hashemi, M. Sawan, and Y. Savaria, "A high-efficiency low-voltage CMOS rectifier for harvesting energy in implantable devices," *IEEE Trans. Biomed. Circuits Syst.*, vol. 6, no. 4, pp. 326–335, Aug. 2012.
- [31] L. Lin, S. Jain, and M. Alioto, "Integrated power management for battery-indifferent systems with ultra-wide adaptation down to nW," *IEEE J. Solid-State Circuits*, vol. 55, no. 4, pp. 967–976, Apr. 2020.
- [32] L. Xia, J. Cheng, N. E. Glover, and P. Chiang, "0.56 V, -20 dBm RF-powered, multi-node wireless body area network system-on-a-chip with harvesting-efficiency tracking loop," *IEEE J. Solid-State Circuits*, vol. 49, no. 6, pp. 1345–1355, Jun. 2014.
- [33] S. Bandyopadhyay and A. P. Chandrakasan, "Platform architecture for solar, thermal, and vibration energy combining with MPPT and single inductor," *IEEE J. Solid-State Circuits*, vol. 47, no. 9, pp. 2199–2215, Sep. 2012.
- [34] S. S. Amin and P. P. Mercier, "MISIMO: A multi-input single-inductor multi-output energy harvesting platform in 28-nm FDSOI for powering net-zero-energy systems," *IEEE J. Solid-State Circuits*, vol. 53, no. 12, pp. 3407–3419, Dec. 2018.
- [35] D. El-Damak and A. P. Chandrakasan, "A 10 nW–1 μW power management IC with integrated battery management and self-startup for energy harvesting applications," *IEEE J. Solid-State Circuits*, vol. 51, no. 4, pp. 943–954, Apr. 2016.
- [36] S. Bandyopadhyay, P. P. Mercier, A. C. Lysaght, K. M. Stankovic, and A. P. Chandrakasan, "A 1.1 nW energy-harvesting system with 544 pW quiescent power for next-generation implants," *IEEE J. Solid-State Circuits*, vol. 49, no. 12, pp. 2812–2824, Dec. 2014.
- [37] M. Choi, I. Lee, T. Jang, D. Blaauw, and D. Sylvester, "A 23pW, 780ppm/ $^{\circ}\text{C}$ resistor-less current reference using subthreshold MOSFETs," in *Proc. ESSCIRC 2014 - 40th Eur. Solid State Circuits Conf.*, 2014, pp. 119–122.
- [38] L. Lin, S. Jain, and M. Alioto, "A 595pW 14pJ/Cycle microcontroller with dual-mode standard cells and self-startup for battery-indifferent distributed sensing," *IEEE Int. Solid-State Circuits Conf. Dig. Tech. Papers*, vol. 61, pp. 44–46, Feb. 2018.
- [39] Y. K. Ramadass and A. P. Chandrakasan, "A battery-less thermoelectric energy harvesting interface circuit with 35 mv startup voltage," *IEEE J. Solid-State Circuits*, vol. 46, no. 1, pp. 333–341, Jan. 2011.
- [40] K. R. Sadagopan, J. Kang, Y. Ramadass, and A. Natarajan, "A cm-Scale 2.4-GHz wireless energy harvester with nanowatt boost converter and antenna-rectifier resonance for wifi powering of sensor nodes," *IEEE J. Solid-State Circuits*, vol. 53, no. 12, pp. 3396–3406, Dec. 2018.
- [41] P. Cao, Y. Qian, P. Xue, D. Lu, J. He, and Z. Hong, "A bipolar-input thermoelectric energy-harvesting interface with boost/flyback hybrid converter and on-chip cold starter," *IEEE J. Solid-State Circuits*, vol. 54, no. 12, pp. 3362–3374, Dec. 2019.



Jiamin Li (Student Member, IEEE) received the B.Eng. degree in electrical engineering from the National University of Singapore (NUS), Singapore, in 2017. She is currently working toward the Ph.D. degree with the Department of Electrical and Computer Engineering, NUS. Her current research interests include body-coupled powering platform, power management and mixed-signal integrated circuits and systems for wearable platforms. Ms. Li was the recipient of the Student Travel Grant Award at ISSCC 2020.



Yilong Dong (Student Member, IEEE) received the B.Eng. degree in electrical engineering from the Dalian University of Technology (DUT), China in 2017. He is currently working toward the Ph.D. degree with the Department of Electrical and Computer Engineering, NUS. His current research interests include body area power transfer circuits and systems for wireless wearable platforms.



Jeong Hoan Park (Member, IEEE) received the B.S. and Ph.D. degrees from the School of Electrical Engineering and Computer Science, Seoul National University, South Korea, in 2011 and 2017 respectively. From 2017 to 2020, he was a Research Fellow with the Electrical and Computer Engineering Department, National University of Singapore, Singapore. He is currently a Staff Engineer with the DRAM Design team, Samsung Electronics, Hwaseong, South Korea. His main research interests topic include developing low-power and low-noise multi-channel bio-signal acquisition and the neural prosthesis with neuromorphic processing SoC. He is also interested in high bandwidth memory (HBM).



Longyang Lin (Member, IEEE) received the dual bachelor's degrees from Shenzhen University, Shenzhen, China and Umeå University, Umeå, Sweden, in 2011 and the master's degree from Lund University, Lund, Sweden, in 2013, and the Ph.D. degree from the National University of Singapore, Singapore, in 2018. He is currently a Postdoctoral Research Fellow with the Department of Electrical and Computer Engineering, National University of Singapore. He has authored or co-authored more than 15 publications on journals and conference proceedings. He is a co-author of the book *Adaptive Digital Circuits for Power-Performance Range beyond Wide Voltage Scaling: From the Clock Path to the Data Path* (Springer, 2020). His research interests include ultra-low power VLSI circuits, self-powered sensor nodes, widely energy-scalable VLSI circuits and general purpose compute-in-memory. Dr. Lin was the recipient of the Student Travel Grant Award at ISSCC 2017 and IEEE SSCS Singapore Chapter Award at 2017 and 2018.



Tao Tang (Member, IEEE) received the B.S. degree from Wuhan University, Wuhan, China, in 2012, and the M.S. and Ph.D. degrees from Nanyang Technological University, Singapore, in 2013 and 2018, respectively, all in electrical engineering. From 2012 to 2017, he was an Attached Research Student with the Institute of Microelectronics, Agency for Science, Technology and Research (A*STAR), Singapore. He has been a Research Fellow with the National University of Singapore, Singapore, since 2017. His research interests include low-noise, high performance readout circuit and system for biomedical applications, and brain machine interfaces.



Jerald Yoo (Senior Member, IEEE) received the B.S., M.S., and Ph.D. degrees with the Department of Electrical Engineering, Korea Advanced Institute of Science and Technology (KAIST), Daejeon, Korea, in 2002, 2007, and 2010, respectively. From 2010 to 2016, he was with the Department of Electrical Engineering and Computer Science, Masdar Institute, Abu Dhabi, United Arab Emirates, where he was an Associate Professor. From 2010 to 2011, he was also with the Microsystems Technology Laboratories (MTL), Massachusetts Institute of Technology (MIT) as a Visiting Scholar. Since 2017, he has been with the Department of Electrical and Computer Engineering, National University of Singapore, Singapore, where he is currently an Associate Professor. He has pioneered researches on low-energy body-area-network (BAN) for communication/ powering and wearable body sensor networks using the planar-fashionable circuit board for a continuous health monitoring system. He authored book chapters in *Biomedical CMOS ICs* (Springer, 2010), *Enabling the Internet of Things—From Circuits to Networks* (Springer, 2017) and *The IoT Physical Layer* (Springer, 2019). His current research interests include low-energy circuit technology for wearable bio-signal sensors, flexible circuit board platform, BAN communication and powering, ASIC for piezoelectric Micromachined Ultrasonic Transducers (pMUT) and System-on-Chip (SoC) design to system realization for wearable healthcare applications. Dr. Yoo is an IEEE Circuits and Systems Society (CASS) Distinguished Lecturer (2019-2021). He was also the IEEE Solid-State Circuits Society (SSCS) Distinguished Lecturer (2017-2018). He was the recipient or a corecipient of several awards including the IEEE International Symposium on Circuits and Systems (ISCAS) 2015 Best Paper Award (BioCAS Track), ISCAS 2015 Runner-Up Best Student Paper Award, Masdar Institute Best Research Award in 2015 and IEEE Asian Solid-State Circuits Conference (A-SSCC) Outstanding Design Award (2005). He was the Vice-Chair of IEEE SSCS United Arab Emirates (UAE) Chapter. Currently, he is a Technical Program Committee Member of the IEEE International Solid-State Circuits Conference (ISSCC), ISSCC Student Research Preview (co-chair), IEEE Custom Integrated Circuits Conference (CICC, Emerging Technologies Subcommittee Chair), and IEEE Asian Solid-State Circuits Conference (A-SSCC, Emerging Technologies and Applications Subcommittee Chair). He is also an Analog Signal Processing Technical Committee Member of IEEE Circuits and Systems Society.